AGU ADVANCING EARTH AND SPACE SCIENCE

Space Weather

RESEARCH ARTICLE
10.1029/2020SW002706

Key Points:

- A novel extended encoder-decoder long short-term memory neural network (ED-LSTME) for ionospheric total electron content (TEC) forecasting over China is developed
- ED-LSTME shows a strong capability in improving TEC forecasting at different geographical locations, seasons, and geomagnetic conditions
- ED-LSTME is robust and outperforms all the six selected baselines when comparing with the models in terms of their performance

Supporting Information:

Supporting Information may be found in the online version of this article.

Correspondence to:

X. Shen,
shenxh@seis.ac.cn

Citation:

Xiong, P., Zhai, D., Long, C., Zhou, H., Zhang, X., & Shen, X. (2021). Long short-term memory neural network for ionospheric total electron content forecasting over China. *Space Weather*, *19*, e2020SW002706. https://doi.org/10.1029/2020SW002706

Received 21 DEC 2020
Accepted 4 MAR 2021

Long Short-Term Memory Neural Network for Ionospheric Total Electron Content Forecasting Over China

Pan Xiong[1], Dulin Zhai[2], Cheng Long[3], Huiyu Zhou[4], Xuemin Zhang[1], and Xuhui Shen[5]

[1]Institute of Earthquake Forecasting, China Earthquake Administration, Beijing, China, [2]Key Laboratory of Earthquake Geodesy, Institute of Seismology, China Earthquake Administration, Wuhan, China, [3]School of Computer Science and Engineering, Nanyang Technological University, Singapore, Singapore, [4]School of Informatics, University of Leicester, Leicester, UK, [5]National Institute of Natural Hazards, Ministry of Emergency Management of China, Beijing, China

Abstract An increasing number of terrestrial- and space-based radio-communication systems are influenced by the ionospheric space weather, making the ionospheric state increasingly important to forecast. In this study, a novel extended encoder-decoder long short-term memory extended (ED-LSTME) neural network, which can predict ionospheric total electron content (TEC) is proposed. Useful inherent features were automatically extracted from the historical TEC by LSTM layers, and the performance of the proposed model was enhanced by considering solar flux and geomagnetic activity data. The proposed ED-LSTME model was validated using 15-min TEC values from GPS measurements over one solar cycle (from January 2006 to July 2018) collected at 15 GPS stations in China. Different assessment experiments were conducted in different geographical locations and seasons as well as under varying geomagnetic activities, to comprehensively evaluate the model's performance. These comparative experiments were conducted using an ED-LSTM, a traditional LSTM, a deep neural network, autoregressive integrated moving average, and the 2016 International Reference Ionosphere models. The results indicated that the ED-LSTME model is superior to the other statistical models, with R^2 and root mean square error values of 0.89 and 12.09 TECU, respectively. In addition, TEC was adequately predicted under different ionospheric conditions, and satisfactory results were obtained even under geomagnetically disturbed conditions. These results suggest that the prediction performance could be significantly improved by utilizing auxiliary data. These observations confirm that the proposed model outperforms several state-of-the-art models in making predictions at different times and under diverse conditions.

1. Introduction

The ionospheric total electron content (TEC) is an important parameter in the study of ionospheric variabilities (Goodman, 1992). Accurate prediction of TEC is critical for the promotion of Earth- and space-based systems such as satellite positioning and remote sensing systems (Belehaki et al., 2009; Samardjiev et al., 1993). Therefore, understanding the spatiotemporal variations in TEC and developing accurate global and regional TEC models are crucial (Kersley et al., 2004).

The International Reference Ionosphere (IRI) model (Bilitza, 2001; Bilitza et al., 2017), NeQuick model (Hochegger et al., 2000; Nava et al., 2008, 2011), Bent model (Bent et al., 1975), and other global empirical models are currently recommended for ionospheric parameter prediction and provide alternative platforms for TEC estimation, including long-term forecasting. However, the instantaneous estimation of the TEC based on "real" measurements is still required. Therefore, estimated TEC values must reflect the real features of observable phenomena in the ionosphere. Consequently, many studies have attempted to develop regional TEC forecasting models to explore ionospheric variability (Badeke et al., 2018; Elmunim et al., 2017; Habarulema et al., 2007; Krankowski et al., 2005; Razin et al., 2015; Tebabal et al., 2019; Watthanasangmechai et al., 2012). In general, methods used to forecast regional TEC can be divided into two major categories: empirical methods (Badeke et al., 2018; J. Li et al., 2020; Mukesh et al., 2020; Mukhtarov et al., 2014) and statistical methods.

However, existing statistical methods used to forecast regional TEC are based on relatively simple theoretical models. Among the existing approaches, Prophet time-series forecasting (Zhai et al., 2019), auto-regressive

moving average (ARMA) (Krankowski et al., 2005; Zhang et al., 2013), statistical Holt–Winter (Elmunim et al., 2017), manifold trajectories (Moreno et al., 2018), support vector machine (Pei et al., 2019), artificial neural network (ANN) (Habarulema et al., 2007), EXtreme Gradient Boosting over Decision Trees (Zhukov et al., 2020), and hybrid methods (Feizi et al., 2020; Ghaffari & Vosooghi, 2020; Mukhtarov et al., 2014; Uwamahoro & Habarulema, 2015) are extensively used. Recently, various neural network (NN)-based models have been developed for the prediction of regional TEC (Tebabal et al., 2018, 2019) A NN is a collection of algorithms modeled after the function of neurons in the brain. In the field of deep computer learning, such networks are often referred to as ANNs and used for classification and prediction purposes (Tebabal et al., 2018).

The results of previous studies suggest that NN models can reflect TEC variations well. A genetic algorithm-based neural network (GA-NN) TEC-prediction model developed for use over China was proposed by Song et al. (2018) and Huang et al. (2015). Its forecasting performance was significantly better than those of the back propagation-based NN (BP-NN) and IRI 2012 models. Okoh et al. (2016) integrated IRI's critical plasma frequency parameter as an additional neuron in the input layer of a regional global navigation satellite system (GNSS)-TEC NN model to monitor Nigeria. The potential extrapolation abilities and the limitations of ANNs were investigated by Habarulema and colleagues, who proposed a regional TEC prediction model for South Africa by determining the relationship between multiple inputs and TEC (Habarulema et al., 2007, 2011). In addition, many hybrid methods involving NN components with high spatiotemporal resolution data have been proposed to model and predict the ionospheric TEC; these include the wavelet NN model (Ghaffari & Voosoghi, 2016), empirical orthogonal function NN model (Uwamahoro & Habarulema, 2015), adaptive NN model with an in situ learning algorithm (Acharya et al., 2011), and Gaussian mixture model-improved NN or radial basis function (RBF) (Huang & Yuan, 2014).

However, the ionospheric TEC is intrinsically complex. Some complex factors that affect forecasting effectiveness such as different geographical locations, seasons, and geomagnetic activities make it difficult to achieve accurate TEC prediction, which requires us to build a more powerful and complex model network. Finally, the data used in most previous studies did not cover a full solar cycle. However, complete solar cycle data coverage is necessary, given the considerable impact of solar activities on the ionospheric dynamics.

Deep learning is considered to be a function of second-generation NNs (Hinton & Salakhutdinov, 2006) and may be employed to better model spatiotemporal variations in ionospheric TEC (Orus Perez, 2019). Hochreiter and Schmidhuber (1997) developed a special deep-learning architecture known as a long short-term memory NN (LSTM NN). LSTM NNs are capable of long-term series learning and are not affected by a vanishing gradient. However, to date, LSTM NNs have been rarely used for ionospheric TEC prediction; their application for a few GPS stations (Ruwali et al., 2020; Srivani et al., 2019) has been attempted only a few times and only to generate a predicted TEC map (Cherrier et al., 2017; Kaselimi et al., 2020); Chen (2019) proposes an improved deep learning algorithm to fill in the TEC map, which shows satisfactory ionospheric peak structures at different times and under different geomagnetic conditions. Therefore, this study aimed to develop an encoder-decoder LSTM extended (ED-LSTME) model to reflect the spatiotemporal relationships between GPS stations and to predict ionospheric TEC. This model was developed and evaluated based on geomagnetic indexes, and measurements were recorded at 15 GPS stations over one solar cycle in China.

2. Data and Data Preprocessing

2.1. Vertical TEC Derivation

All GPS stations provide pseudorange and carrier phase measurements at two L-band frequencies. The difference between the code and carrier phase measurements of the two frequencies was calculated to obtain the pseudorange TEC ($STEC_a$) and phase TEC ($STEC_r$) along the path from a satellite to a receiver (Mannucci et al., 1998). The formula of the pseudorange TEC is as follows:

$$\mathrm{STEC}_a = \frac{f_1^2 f_2}{A\left(f_1^2 - f_2^2\right)}\left[\left(P_1 - P\right)_2 - c\left(b^{s,1} - b^{s,2}\right) - c\left(b_{r,1} - b_{r,2}\right)\right], \quad (1)$$

where $A = 40.3\ m^3/s^2$; f_1 and f_2 are GPS signal frequencies; P_1 and P_2 indicate the respective recorded pseudo ranges; c is the speed of light; and $b^{s,1}-b^{s,2}$ and $b_{r,1}-b_{r,2}$ are the Differential Code Biases for the satellite and receiver, respectively. The Differential Code Bias must be estimated by eliminating the differences between the ionospheric delays of the corresponding observations (Z. Li et al., 2012; Yuan et al., 2015). The TEC phase is expressed as follows:

$$\mathrm{STEC}_r = \frac{f_1^2 f_2}{A\left(f_1^2 - f_2^2\right)}\left[\left(\frac{c\phi_1}{f_1} - \frac{c\phi_2}{f_2}\right) - \left(\lambda_1 N_{r,1}^s - \lambda_2 N_{r,2}^s\right)\right], \tag{2}$$

where ϕ_1 and ϕ_2 are the carrier phases; λ_1 and λ_2 indicate the wavelengths; and $\lambda_1 N_{r,1}^s - \lambda_2 N_{r,2}^s$ is the integer cycle ambiguity. The Differential Code Bias and integer cycle ambiguity were regarded as constant within a period, assuming that the cycle slip does not disrupt the continuity of observation. Based on the STECa, a more accurate slant TEC (STEC_i) could be acquired by smoothing the STECr at a certain time i during continuous measurements of N epochs (Hernández-Pajares et al., 2011, 2012).

$$\mathrm{STEC}_i = \mathrm{STECr}_i + \frac{1}{N}\sum_{i=1}^{N}\left(\mathrm{STECa}_i - \mathrm{STECr}_i\right) \tag{3}$$

The slant TEC was converted into the vertical TEC (VTEC) to allow the convenient examination of the distribution of TEC in different regions. This conversion was achieved using a mapping function at different ionospheric pierce points (IPPs), which are the points of intersection between the line of sight and the ionospheric shell. The charged particles of the ionosphere are assumed to be concentrated in a thin shell concentric with the earth, and this thin layer is located in the ionosphere. The shell's height above the ground varies based on the time of day or night, geographical location, sun zenith angle, and other factors; typical values range from 350–480 km and can be rapidly calculated. When the elevation angle exceeds 30°, the calculation yields highly accurate results and is suitable for application in most areas of the world. The VTEC is obtained via the equation below (Afraimovich et al., 2001; Hernández-Pajares et al., 2011).

$$\mathrm{VTEC} = \mathrm{STEC} \times \sqrt{1 - \left(\frac{R_E \cos E_0}{R_E + h_m}\right)^2}, \tag{4}$$

where R_E represents the average radius of the Earth; h_m represents the F2 layer peak height; E_0 indicates the elevation angle of the satellite station (Xiong et al., 2014, 2016).

In this study, we used dense GNSS observation station data to fix the satellite Differential Code Biases (DCB), assuming that the vertical TEC over the grid point within a certain time and space were equal and that the vertical TEC over the grid and the hardware delay of the GNSS system were solved simultaneously through the observation equation (Choi et al., 2011; Ma & Maruyama, 2003), The specific equation used is as follows:

$$\begin{aligned}
\mathrm{TECS1} &= \mathrm{GridTECV1} + B_{r1} + B^{S1}\\
\mathrm{TECS2} &= \mathrm{GridTECV1} + B_{r2} + B^{S1}\\
\mathrm{TECS3} &= \mathrm{GridTECV1} + B_{r3} + B^{S1}\\
\mathrm{TECS4} &= \mathrm{GridTECV1} + B_{r1} + B^{S2}\\
\mathrm{TECS5} &= \mathrm{GridTECV1} + B_{r2} + B^{S2}\\
\mathrm{TECS6} &= \mathrm{GridTECV1} + B_{r3} + B^{S2}\\
&\ldots
\end{aligned} \tag{5}$$

Among them, B^{Si} is the hardware delay between different frequency signals of the ith satellite, and B_{rj} is the hardware delay between different frequency signals of the jth receiver. The vertical TEC is based on the technique of Ma and Maruyama (2003) involving mapping and all data obtained from the Crustal Movement Observation Network of China were used. In the above approach, we used a zero-mean condition for the

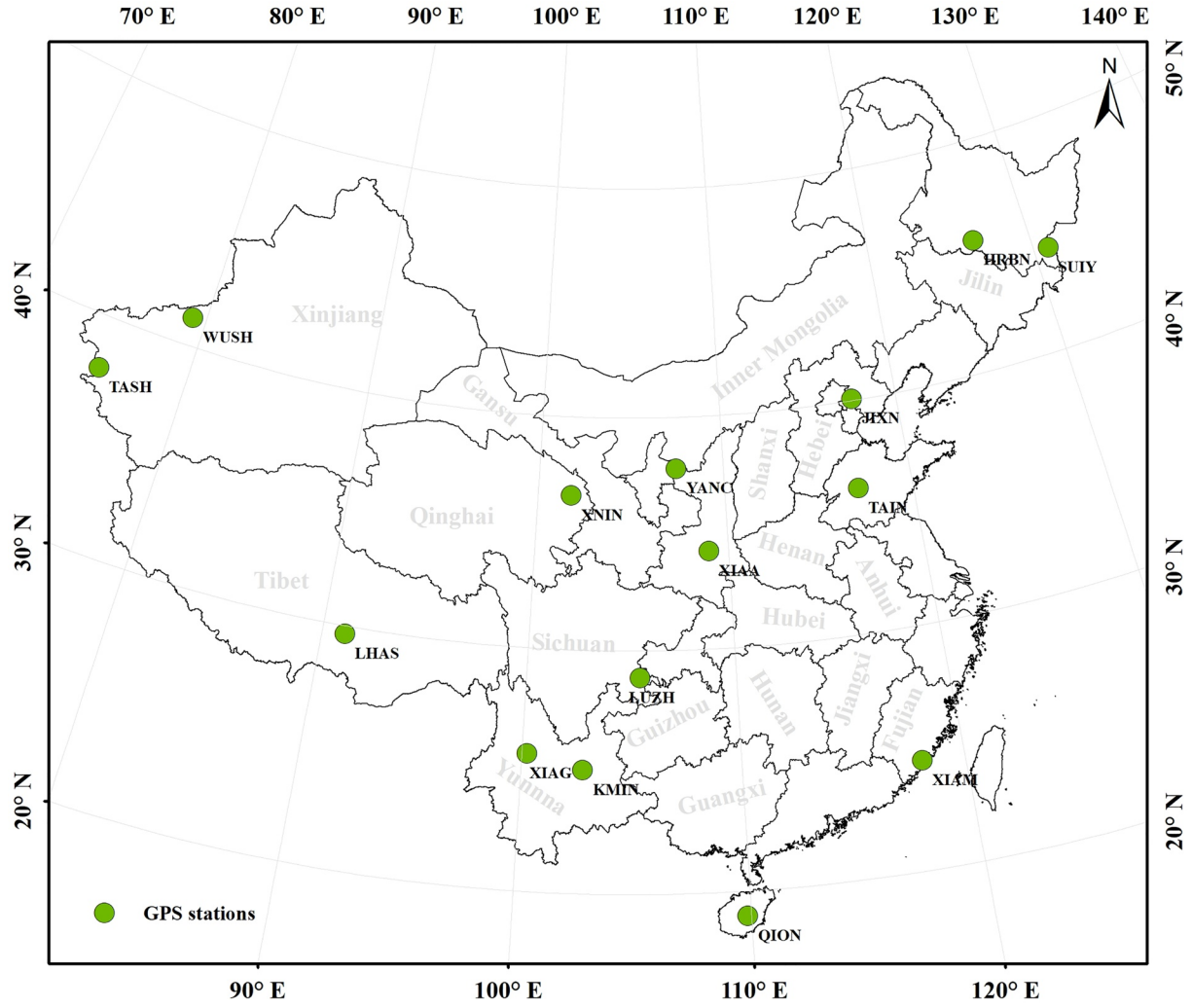

Figure 1. Study region and spatial distribution of GPS stations.

separation of the receiver-dependent part of the bias. In practice, the singular value decomposition (SVD) method was used to estimate DCB, a more detailed description of the method is given in Choi et al. (2011).

2.2. Data Collection and Preprocessing

In this study, GPS TEC data were obtained from the Crustal Movement Observation Network of China (CMONOC), which consists of 260 GNSS stations covering mainland China. As geographical location affects TEC estimation and data from evenly distributed stations can better reflect the geographic variability in the model performance, this study focuses on 15 stations evenly distributed throughout China (Figure 1). Table 1 lists the geographic locations of the 15 GPS stations that were used to construct and validate the model.

The data include three main parts, including (1) vertical TEC values with a temporal resolution of 15 min were obtained from dual-frequency (1575.42 and 1227.6 MHz) observations (Mannucci et al., 1998); (2) The geomagnetic index a_p was used as an indicator of the overall geomagnetic activity and magnetic storms. The magnetic effect of the K_p index was utilized to measure solar particle radiation. Bartels introduced the three-hour-range K_p index in 1949 (Bartels & Veldkamp, 1949); the data can be downloaded from http://wdc.kugi.kyoto-u.ac.jp. (3) Finally, the F10.7 index, the solar radio flux at 10.7 cm (2800 MHz), was used owing to its excellence and consistency as an indicator of solar activities.

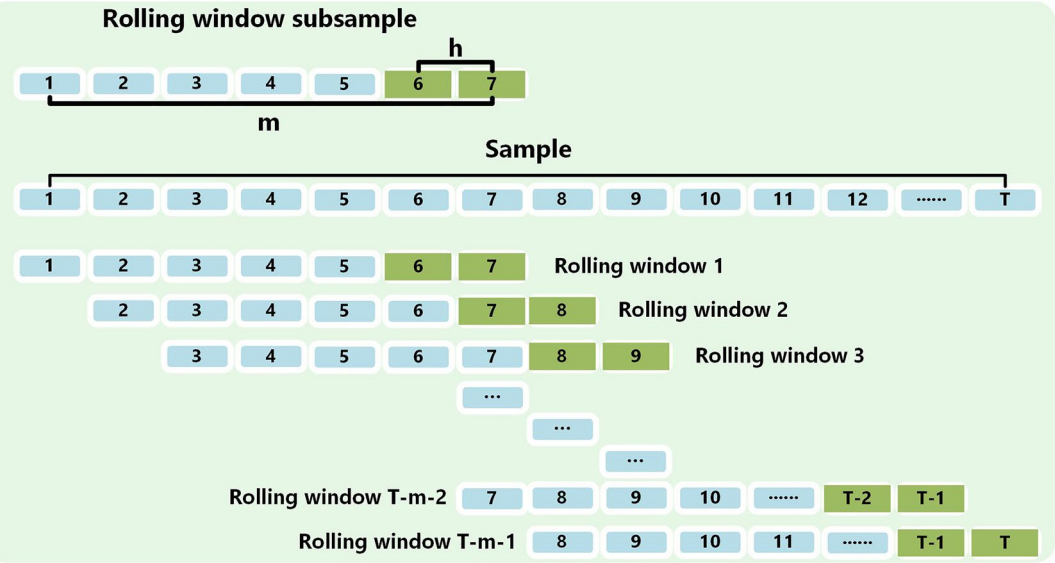

Figure 2. Rolling-window partitions.

We calculated the mean and standard deviation of the TEC time series for each station and then calculated appropriate thresholds to identify and exclude outliers, which were considered as values that were more than three standard deviations from the mean. To fill in the removed and missing data, we opted for an approach drawn from statistics and control theory called Kalman smoothing, which is available in the imputeTS package (Moritz, 2016) in R. The Kalman filter takes a forward pass through the data up to the current time point and can be applied in real-time. Kalman smoothing adds a backward pass through the data, thereby using all the data. After the data preprocessing and integration, a total of 2,632,410 records was collected for model development (175,494 records for each station).

This study covered a period of 12.5 years (January 2006 to April 2018). The training sets were used as input parameters, and TEC values from January 2006 to December 2016 were used, representing the period of one solar cycle. The model performance was verified using data from the same stations from January 2017 to April 2018 as validation datasets.

2.3. Time Series Sample Modeling

Preprocessing was conducted after data acquisition, including sample modeling, which is an essential step for time-series data preprocessing. The data can be converted using a machine-learning or deep-learning model. For time series problems, the sliding window is a representative modeling technique and was used in this study (Zivot & Wang, 2003).

Based on the assumption that samples and data were available for all periods, sliding windows were used for back tests to check the prediction ability of several series models. Back testing involves the following steps:

1. Select the size of the sliding window, m (i.e., the number of consecutive observations per sliding window), which depends on the sample size, T, and periodicity of the data
2. Select the prediction horizon, h, which depends on the application and the periodicity of the data. Figure 2 shows how the sliding window segregates the time series
3. If the number of increments between consecutive windows is 1 period, the overall data set is segregated into $N = T-m+1$ subsamples. The first window includes the views of period (1, m), the second window contains period (2, $m+1$), and so on (Figure 2)
4. Regarding the subsamples of each window
   a) build every model
   b) estimate the h−step−ahead predictions

Table 1
List of GPS Stations With Geographic Coordinates

	Station code	Station name	Province (city)	Geographic latitude	Geographic longitude	Geomagnetic latitude	Geomagnetic longitude
High latitude	WUSH	Ush	Xinjiang	41.200°N	79.210°E	32.58°N	155.04°E
	HRBN	Harbin	Heilongjiang	45.700°N	126.620°E	36.56°N	163.24°W
	TASH	Tashkurgan	Xinjiang	37.770°N	75.230°E	29.47°N	151.08°E
	SUIY	Suiyang	Heilongjiang	44.43°N	130.91°E	35.51°N	159.38°W
Middle latitude	YANC	Yanchi	Ningxia	37.780°N	107.440°E	28.18°N	179.89°W
	LUZH	Luzhou	Sichuan	28.870°N	105.410°E	19.30°N	178.22°E
	XNIN	Xining	Qinghai	36.600°N	101.770°E	27.05°N	174.99°E
	JIXN	Jixian	Tianjin	40.080°N	117.530°E	30.61°N	170.91°W
	TAIN	Tai'an	Shandong	36.210°N	117.120°E	26.74°N	171.13°W
	XIAA	Xi'an	Shanxi	34.180°N	108.990°E	24.60°N	178.48°W
	LHAS	Lhasa	Tibet	29.660°N	91.100°E	20.43°N	164.96°E
Low latitude	XIAG	Xiaguan	Yunnan	25.610°N	100.250°E	16.12°N	173.36°E
	XIAM	Xiamen	Fujian	24.450°N	118.080°E	15.05°N	169.85°W
	KMIN	Kunming	Yunnan	25.030°N	102.800°E	15.50°N	175.75°E
	QION	Qiongzhong	Hainan	19.030°N	109.850°E	9.51°N	177.57°W

c) calculate the prediction error for each prediction; $e_{nj} = y_{m-h+n+j} - \hat{y}_{nj}$, where
   - e_{nj} represents the prediction error of window n for the $j-$step$-$ahead prediction
   - y is the response, and
   - $\hat{y}_{nj}$ represents the $j-$step$-$ahead prediction of window subsample n

5. Calculate the root mean square error (RMSE) values according to the prediction error for each step-ahead prediction type
6. Compare the RMSEs of these models. The model with the lowest RMSE is considered to yield the best prediction performance

3. Methodology

3.1. ED-LSTME Model

The LSTM, a type of recurrent NN, was specifically designed to prevent the attenuation or explosion of model output when a given input is circulated through a feedback loop (Hochreiter & Schmidhuber, 1997). It can effectively model time dependencies and has been utilized in many fields include meteorology (Hu & Chen, 2018; Qing & Niu, 2018), network traffic (Zhao et al., 2017), and air-pollution forecasting (Yang et al., 2020).

However, the lengths of the input and output sequences in the LSTM model may differ, which could lead to vanishing and explosion gradients. The ED-LSTM has been established as an effective means to address these prediction problems (Cho et al., 2014). The key advantage of this model is that it can be easily constructed with little more than a list of inputs and outputs. The ED-LSTM consists of two models; the first is used to read the input sequence and encode it into a fixed-length vector, and the second is used to decode the fixed-length vector and output the predicted sequence.

In this study, an encoder-decoder LSTM NN was used to predict the regional TEC. In general, encoder-decoder LSTM models are used to map input and output sequences of arbitrary lengths (Sutskever et al., 2014). The encoder component can be obtained by applying one or more LSTM layers, and the model output is a vector of a fixed size (i.e., the internal representation of the input sequence) defined by the number of

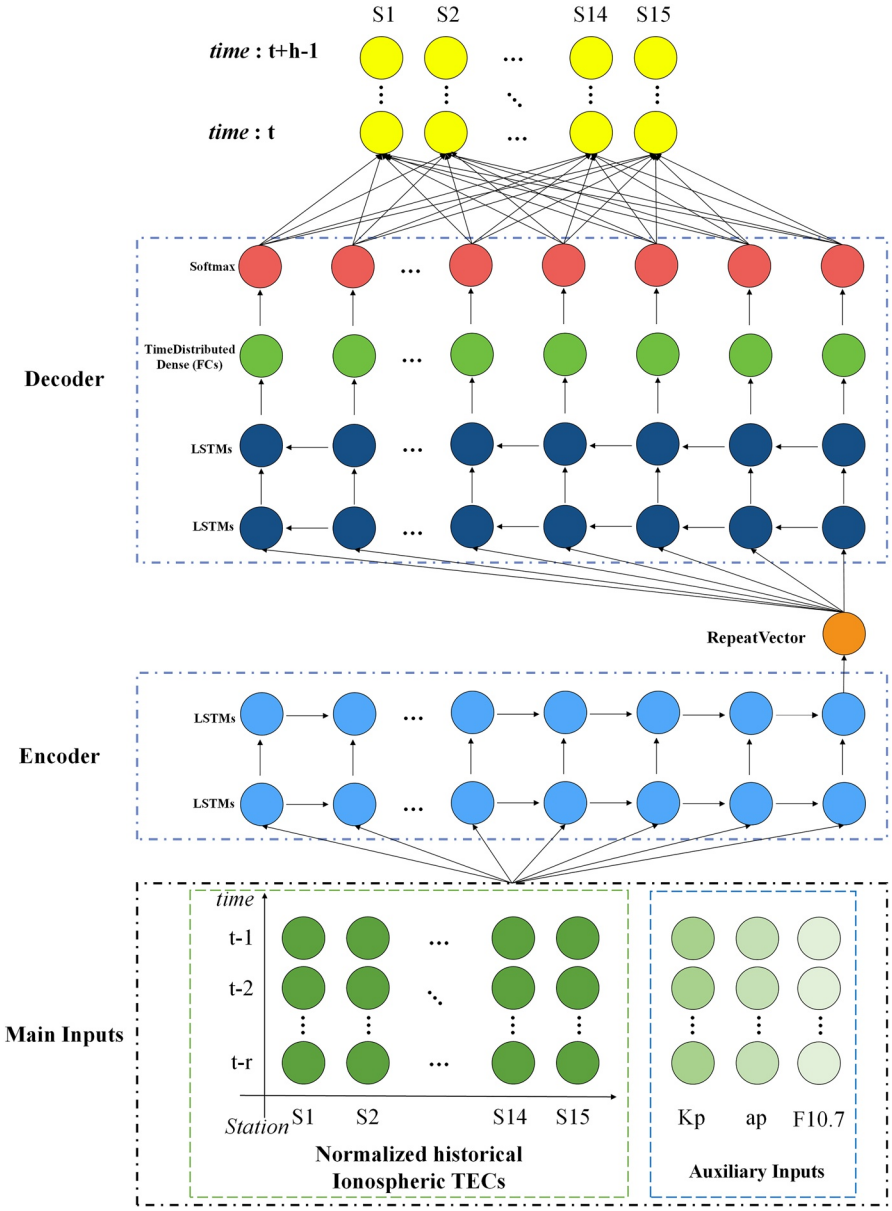

Figure 3. Network framework of the ED-LSTME model for TEC prediction. The main inputs (historical ionospheric TECs) are in the green dashed boxes, and auxiliary inputs (geomagnetic activity index K_p and a_p; solar activity index F10.7) are in blue dashed boxes; r represents the time lag, and h is the forecast horizon. ED-LSTME, encoder-decoder long short-term memory extended; TEC, total electron content.

memory cells in the layer. The decoder component can also be implemented using one or more LSTM layers and converts the internal representation into the correct output sequence. Thus, the fixed-sized output of the encoder model is read using the decoder.

In the ED-LSTME model, we propose (shown in Figure 3), representative features were extracted from historical TEC data and auxiliary input data via LSTM layers. The dense layer in a TimeDistributed wrapper (Chollet, 2017) was utilized as the network output, and the RepeatVector layer (Chollet, 2017) served as an adapter for both the network's encoding and decoding sections (the RepeatVector can be deployed to repeat the fixed-length vector once at each time step in the output sequence). We implemented the ED-LSTME model using the Keras (https://github.com/fchollet/keras available from GitHub) (Chollet, 2015)

open-source deep learning framework with TensorFlow (Abadi et al., 2016) as the backend, open-source software for the development of NN models.

Previous studies have shown that solar and geomagnetic activities affect TEC variability (Blagoveshchensky et al., 2018; Kumar & Singh, 2010; Purohit et al., 2015; Verkhoglyadova et al., 2013) and that the use of auxiliary solar and geomagnetic activity index data potentially improves prediction performance. Specifically, time-delayed historical data and current auxiliary data of the solar flux index K_p and geomagnetic activity index a_p from all selected GPS stations were concatenated and stacked to compose an input sequence for the LSTM layers ("Main Inputs" in Figure 3).

The encoder LSTM layers process the input sequence and generate a summary of the past input sequence through the unit-state vector. After N recursive updates, the encoder LSTM layers convert the overall input sequence into the final unit-state vector. The encoder then passes the vector to the decoder LSTM, which uses it as the initial unit state for sequence generation. The decoder LSTM then recursively generates the output sequence. Subsequently, further representations of the merged features are obtained by utilizing one or more fully joined layers ("FCs" in Figure 3). Finally, the prediction output is produced based on the fully joined layer.

3.2. Parameter Optimization

Better results can be obtained by adjusting the ED-LSTME model parameters (i.e., the number of neurons in every LSTM layer N_N^{LSTM}, number of neurons in every FC layer N_N^{FC}, number of training epochs N_N^{EPOOCHS}, and batch size). As this study aimed to discuss TEC prediction at different time granularities, and the optimum sliding window size (including the time lag and forecast horizon) varies for different granularities, the parameters L_N^{Lag} (the length of the time lag for the input) and L_N^{Horizon} (the length of the forecast horizon for the output; that is, 1 per 15 min, 4 per hour, etc.) needed to be optimized.

Based on the empirical results, the parameter candidates were set as follows: $\left\{N_N^{\mathrm{LSTM}}, N_N^{\mathrm{FC}}\right\} = \{100, 200, 300, 400\}$, batch size = {32, 64, 128}, $N_N^{\mathrm{EPOOCHS}} = \{50, 100\}$, $L_{\mathrm{N}}^{\mathrm{Lag}} = \{96, 2 * 96, 3 * 96\}$, and $L_N^{\mathrm{Horizon}} = \{8, 12, 16\}$. The mini-batch gradient descent, dropout neuron, and L2 regularization algorithms were combined to optimize the parameters, and the RMSE was used as an optimization criterion.

$$\mathrm{RMSE} = \sqrt{\frac{1}{n}\sum_{i=1}^{n}\left(y_i - y_i^*\right)^2} \tag{6}$$

where y_i represents the observed value of the ith case, and y_i^* is the predicted value. A smaller RMSE indicates better performance.

Hyperparametric optimization trials (Data Set S1 in the Supplementary Materials) were conducted. After several rounds of grid searching, an optimal result was yielded with an RMSE value of 12.09 TECU when using the following parameters: $\left\{N_N^{\mathrm{LSTM}}, N_N^{\mathrm{FC}}\right\} = 300$, batch size = 128, $N_N^{\mathrm{EPOOCHS}} = 50$, $L_N^{\mathrm{Lag}} = 96$ (1 d), and $L_N^{\mathrm{Horizon}} = 12$ (3 h).

3.3. Model Comparison

To assess its performance, the performance of the proposed model was compared with those of other algorithms such as the classic ED-LSTM, ordinary LSTM (Hochreiter & Schmidhuber, 1997), deep neural network (DNN) (Goodfellow et al., 2016; LeCun et al., 2015), autoregressive integrated moving average (ARIMA) (Hyndman & Athanasopoulos, 2018; Makridakis & Hibon, 1997), and IRI 2016 models (Bilitza, 2018; Rawer et al., 1978). Hyperparametric optimization, which is used in all the methods except for IRI 2016, allow for the identification of the optimum parameters. Based on this optimization, relevant technology can be selected with high confidence, ensuring the use of a robust method. For the classic ED-LSTM, ordinary LSTM, and DNN models, the hyperparameters of the neuron number in every LSTM

Table 2
Performance of the Tested Models

Models	R^2	MAE	RMSE	ρ
ED-LSTME	0.8862	3.6967	12.0954	0.9416
Encoder-decoder LSTM	0.5462	5.1447	24.1536	0.8209
LSTM	0.3469	5.3384	28.9778	0.6984
DNN	0.2784	5.6924	30.4596	0.5411
ARIMA	0.0689	6.1995	34.5988	0.2859
IRI 2016	0.0643	5.8312	34.6854	0.3143

Abbreviations: ARIMA, autoregressive integrated moving average; DNN, deep neural network; ED-LSTME, encoder-decoder long short-term memory extended; IRI, International Reference Ionosphere; LSTM, long short-term memory; MAE, mean absolute error; RMSE, root mean square error.

and FC layer, training epoch number, and batch size were selected for model optimization. The optimized ARIMA model was obtained by applying the Hyndman-Khandakar algorithm (Hyndman & Khandakar, 2008) for automatic modeling based on the combination of unit root tests, the minimization of the Akaike information criterion (AICc), and maximum likelihood estimation (MLE). Hyperparametric optimization trials conducted for these models are described in Datasets S1 of the Supplementary Material. In addition, the degrees of freedom (the number of parameters in the model) for the proposed ED-LSTME model; the encoder-decoder LSTM model; the LSTM, DNN, and ARIMA models; and the IRI 2016 model were 140116, 138916, 226992, 235292, 8, and 28, respectively.

To assess the performance of the various models, four different statistical indicators were used in this study: RMSE, the coefficient of determination (R^2), mean absolute error (MAE), and the correlation coefficient (ρ), given by Equations 6–9, respectively. MAE refers to the absolute error between the true value and the predicted value. RMSE is the square of the difference between the true value and the predicted value. When MAE and RMSE are used together, the degree of dispersion of the sampling error can be seen. The correlation coefficient is used to describe the degree of linear correlation between two variables. The *R*-square is generally used in regression models to evaluate the degree of agreement between the predicted value and the actual value.

$$R^2 = \left(\frac{\sum_{i=1}^{n} \left(y_i - \overline{y}\right)\left(y_i^* - \overline{y^*}\right)}{\sqrt{\sum_{i=1}^{n} \left(y_i - \overline{y}\right)^2} \sqrt{\sum_{i=1}^{n} \left(y_i^* - \overline{y^*}\right)^2}} \right)^2 \tag{7}$$

$$\mathrm{MAE} = \frac{1}{n} \sum_{i=1}^{n} \left| y_i - y_i^* \right| \tag{8}$$

$$\rho = \frac{\sum_{i=1}^{n} \left(y_i^* - \overline{y^*}\right)\left(y_i - \overline{y}\right)}{\sqrt{\sum_{i=1}^{n} \left(y_i^* - \overline{y^*}\right)^2 \sum_{i=1}^{n} \left(y_i - \overline{y}\right)^2}}, \tag{9}$$

where n is the number of cases, y_i is the observed value of the ith case, y_i^* is the predicted value, and $\overline{y}$ and $\overline{y}^*$ are the mean values of y_i and y_i^*, respectively.

4. Results and Discussion

4.1. Model Performance

The performance of the various models is detailed in Table 2. The R^2 and RMSE values varied from 0.0643 to 0.8862 and 12.09 to 34.69 TECU, respectively. Based on the use of the international standard empirical model for the terrestrial ionosphere, the IRI 2016 (Bilitza, 2018) model delivered the worst performance, with an R^2 value of 0.0643. The ARIMA model, which is a traditional time-series forecasting method, also performed poorly ($R^2 = 0.068$). An improved R^2 value (0.0689–0.2784) was obtained for the DNN model, indicating that the model's three fully connected layers delivered better performance. As the LSTM model could almost seamlessly deal with scenarios including multiple input variables, it delivered significantly improved performance compared with that of the DNN model, with an increase of 0.06 for R^2 and a decrease of 1.48 TECU for RMSE.

As an intelligent algorithm, the encoder-decoder LSTM model offered better TEC prediction, with R^2 and RMSE values of 0.5462 and 24.1536 TECU, respectively. The ED-LSTME model was superior to the standard ED-LSTM owing to its consideration of space environment information. The ED-LSTME R^2 value increased by 0.34 over that of the standard ED-LSTM (from 0.5462 to 0.8862) and the RMSE value decreased by 12.06 TECU (from 24.1536 to 12.0954 TECU). These findings indicate that the proposed ED-LSTME model delivered the best performance among the considered models, followed by that of the encoder-decoder LSTM, LSTM, DNN, ARIMA, and IRI 2016 models.

While conventional models (e.g., ARIMA) have delivered reasonable results under geomagnetically quiet conditions (Xiaohong et al., 2014; Zhang et al., 2013), they did not deliver the expected performance on a larger scale, with R^2 and RMSEs values of 0.0689 and 34.5988 TECU, respectively. However, the R^2 and RMSEs values ranged from 0.2784 to 0.8862 and from 12.0954 to 30.4596 TECU, respectively. Therefore, the more advanced models (ED-LSTME, encoder-decoder LSTM, LSTM, and DNN) demonstrated better TEC estimation performance.

As the superiority of the ED-LSTME model was confirmed under the study scenario, the performance of the model was further evaluated. The model's efficiency was investigated using Taylor diagrams (Elvidge et al., 2014; Taylor, 2001) (Figure 4). The diagram shows that the ED-LSTME model performed significantly better than did the other models, as ED-LSTME has a stronger correlation to the expected results and a smaller standard deviation than those of the other models. The error standard deviation of IRI 2016 was larger than those of the more advanced models (ED-LSTME, encoder-decoder LSTM, LSTM, and DNN) and ARIMA (albeit only slightly). The standard deviation values for encoder-decoder LSTM, IRI 2016, and DNN were similar and were superior to those of ARIMA and LSTM. Compared with those of the other methods, the standard deviation of the TEC values predicted using the ED-LSTME model displayed very little bias. Thus, based on a consideration of the collective results, the ED-LSTME model significantly outperformed the other models.

In addition, from the International GNSS Service (https://www.igs.org), the global ionospheric TEC levels from January 2017 to April 2018 were relatively low, with an average of around 12 TECU. To prove our proposed model has better generalization ability during higher ionospheric activity, we select the relatively high value in the test set (TEC values greater than 20 TECU) and their corresponding predicted values, and conducted a comparative study. From Figure S3, it can be concluded that while the prediction performance of other models is worse than before, the ED-LSTME not only performs best in the error standard deviation and correlation, but also is the best model in bias. These results show that the ED-LSTME has good generalization ability.

4.2. Variation of Model Performance With Geographical Location

Geographical location affects TEC estimation. Therefore, models were established for each station to determine the geographic variability in the model performance. Table 1 provides the geographical coordinates of the stations, and Tables S1 and S2 present the overall evaluation results for the ED-LSTME, encoder-decoder LSTM, LSTM, DNN, ARIMA, and IRI 2016 models for each station.

For example, at HRBN station, the RMSE of the ED-LSTME model was 1.4547 TECU (i.e., smaller than those of the encoder-decoder LSTM (1.5011 TECU), LSTM (1.7932 TECU), DNN (1.8883 TECU), ARIMA (2.3696 TECU), and IRI 2016 (2.3837 TECU) models). The ED-LSTME model exhibited an R^2 value of 0.7466, which was higher than those of the encoder-decoder LSTM (0.7301), LSTM (0.6149), DNN (0.5129), ARIMA (0.3275), and IRI 2016 (0.3195) models.

Using the ED-LSTME model, the largest R^2 values were obtained at YANC station (0.8311; middle latitude) and KMIN station (0.8052; low latitude), and the smallest value was obtained at SUIY station (0.4247, high latitude). The minimum and maximum correlation coefficients were also obtained at YANC and KMIN stations, respectively. The largest correlation coefficient of 0.912 was obtained at YANC station, whereas the smallest correlation coefficient of 0.7339 was obtained at SUIY station. The encoder-decoder LSTM, LSTM, DNN, ARIMA, and IRI 2016 models yielded R^2 values and correlation coefficients of 0.4091–0.7861 and 0.7299–0.8905, 0.3303–0.7805 and 0.6532–0.8869, 0.207–0.7429 and 0.4951–0.8853, 0.0389–0.7264 and 0.0869–0.8641, and 0.0302–0.6586 and 0.3545–0.8631, respectively.

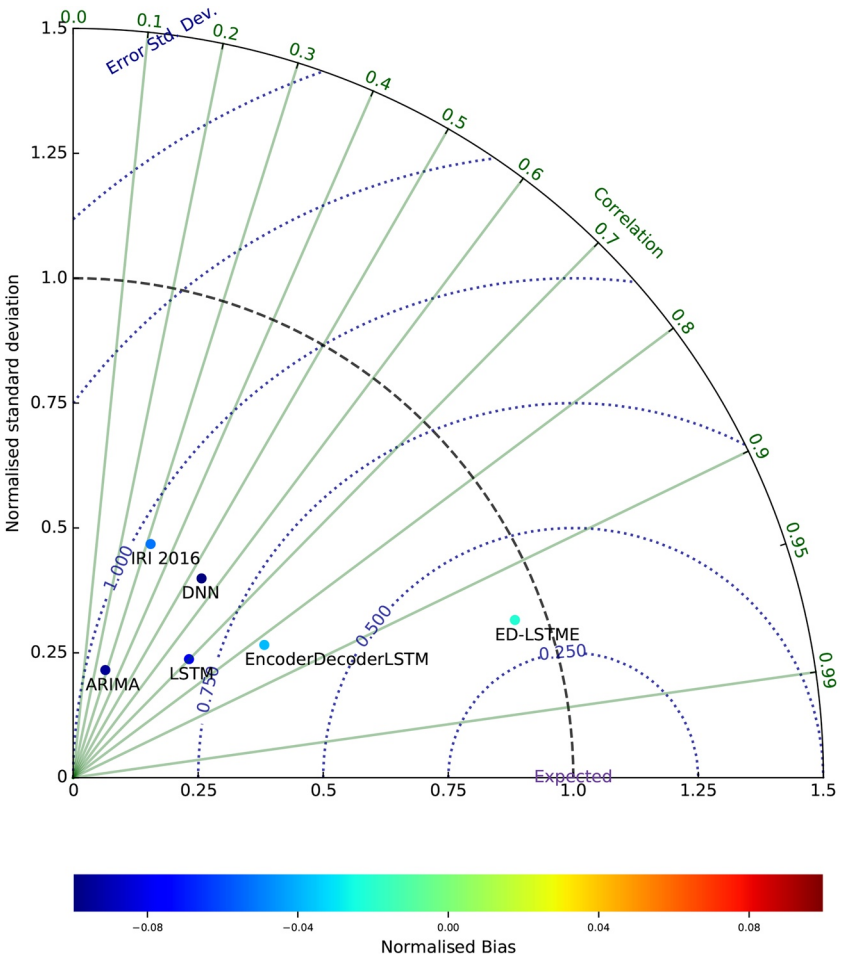

Figure 4. Taylor diagram of model bias and standard deviation of errors. The azimuth indicates the correlation, the radial distance represents the standard deviation, and the semicircles centered on the "Expected" label represent the error standard deviation. The color scale represents the degree of bias. Each quantity was standardized to draw multiple parameters. The appropriate "factors" in the upper right of the chart can be utilized to modify the original values. The chart presents the performances of the ED-LSTME, encoder-decoder LSTM, LSTM, DNN, ARIMA, and IRI 2016 models. ARIMA, autoregressive integrated moving average; DNN, deep neural network; ED-LSTME, encoder-decoder long short-term memory extended; IRI, International Reference Ionosphere; LSTM, long short-term memory.

Figure 5 presents the calculated RMSE values for the correlation between the observed and estimated TEC values, which can be used to further analyze the spatial performances of the models. As shown in the figure, the RMSEs of all six models were lower in the middle and high latitudes. This can possibly be explained by the equatorial ionospheric anomaly (EIA) in lower latitudes, which may lead to larger RMSEs as suggested by Song et al. (2018).

In addition, the R^2 (upper left), MAE (upper right), RMSE (lower left), and ρ (lower right) of the six models are compared in the bar chart in Figure 6. Notably, the ED-LSTME model had the highest prediction efficiency and outperformed the other five models across latitudes.

4.3. Seasonal Variation in Model Performance

Previous studies indicated TEC prediction model performance varies seasonally (Mukesh et al., 2020; Ruwali et al., 2020; Song et al., 2018; Tebabal et al., 2018, 2019). Therefore, all considered models were operated in each season to investigate their performance throughout the solar year. The seasons were delineated as spring (March–May), summer (June–August), autumn (September–November), and winter (December–February), for which the number of data records was 138,240, 139,776, 141,312, and 141,312 respectively.

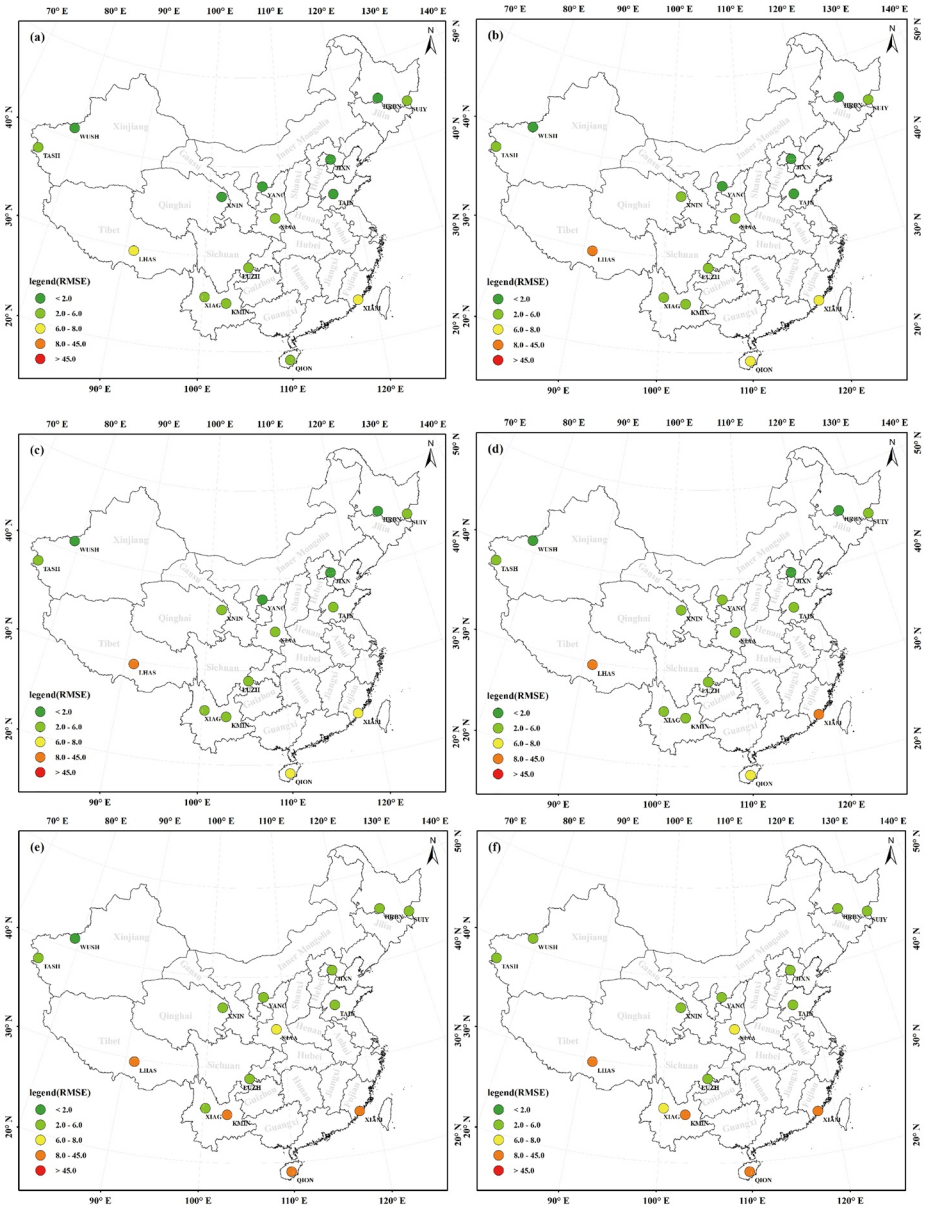

Figure 5. Spatial differences in the RMSE value between observed and estimated TEC values over GPS stations in China. (a) ED-LSTME model; (b) encoder-decoder LSTM model; (c) LSTM model; (d) DNN model; (e) ARIMA model; (f) IRI 2016 model. ARIMA, autoregressive integrated moving average; DNN, deep neural network; ED-LSTME, encoder-decoder long short-term memory extended; IRI, International Reference Ionosphere; LSTM, long short-term memory; RMSE, root mean square error.

Figure 7 presents the seasonal variations in model performance using the testing data. Tables S3 and S4 list the R^2, MAE, RMSE, and correlation coefficient (ρ) values for the predicted TEC and seasonal variations in these values, respectively.

Tables S3 and S4 indicate that the ED-LSTME model delivered the best performance in each season (R^2 = 0.8209, 0.8425, 0.8769, and 0.9066 for the testing data from spring, summer, autumn, and winter, respectively). It was followed by the encoder-decoder LSTM, LSTM, DNN, and ARIMA models (R^2 values of 0.7332, 0.7963, 0.0659, and 0.0204, respectively); the IRI 2016 model delivered the worst performance. This indicates that relatively advanced models achieved significantly better TEC-estimation accuracy than did simpler models based on their consideration of more space environment parameters.

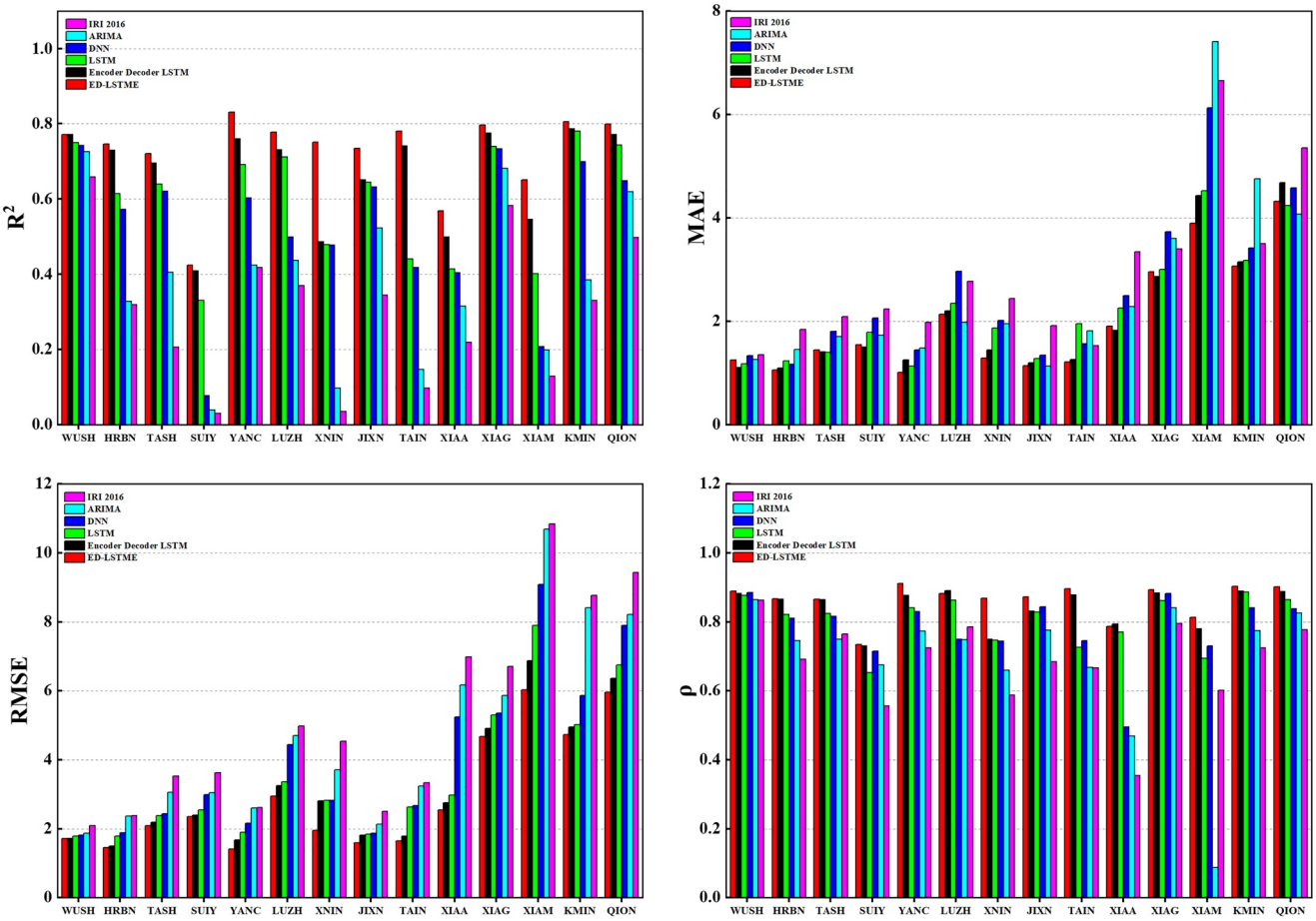

Figure 6. Bar graph illustrating the R^2 (upper left), mean absolute error (MAE; upper right), root mean square error (RMSE; lower left), and correlation coefficient (ρ; lower right) between the measured and predicted TEC values estimated using the ED-LSTME, encoder-decoder LSTM, LSTM, DNN, ARIMA, and IRI 2016 models. ARIMA, autoregressive integrated moving average; DNN, deep neural network; ED-LSTME, encoder-decoder long short-term memory extended; IRI, International Reference Ionosphere; LSTM, long short-term memory; TEC, total electron content.

In addition, despite outperforming the conventional methods, the performance of the DNN model was slightly inferior to those of the LSTM-based models in each season; this suggests that the LSTM models could learn (or "remember") larger temporal dependence and to perform well in time-series forecasting. Overall, prediction error was largest in winter, although the winter TEC is smaller than those in spring and summer. This may reflect the effects of solar activities.

The performances of most models on the seasonal scale were considerably better than those on the annual scale, thus highlighting the effect of seasons on TEC estimation. The R^2 values obtained using conventional models (DNN, ARIMA, and IRI 2016) at the seasonal scale (especially in spring and summer) were significantly improved over those obtained at the annual scale, thus verifying that conventional models are more appropriate for seasonal observations.

4.4. Variation in Model Performance Owing to Solar and Geomagnetic Activity

To further investigate the prediction abilities of the proposed models under varying ionospheric conditions at diverse locations and times, the TEC values obtained on quiet days ($K_p < 3.0$ or $a_p < 56$) and under disturbed conditions ($K_p > 3.0$ or $a_p > 56$) were compared. The geomagnetic activity indices K_p and a_p were utilized to determine the quietest and most disturbed days of every month, as it is known that ionospheric variability significantly increases during geomagnetic activity.

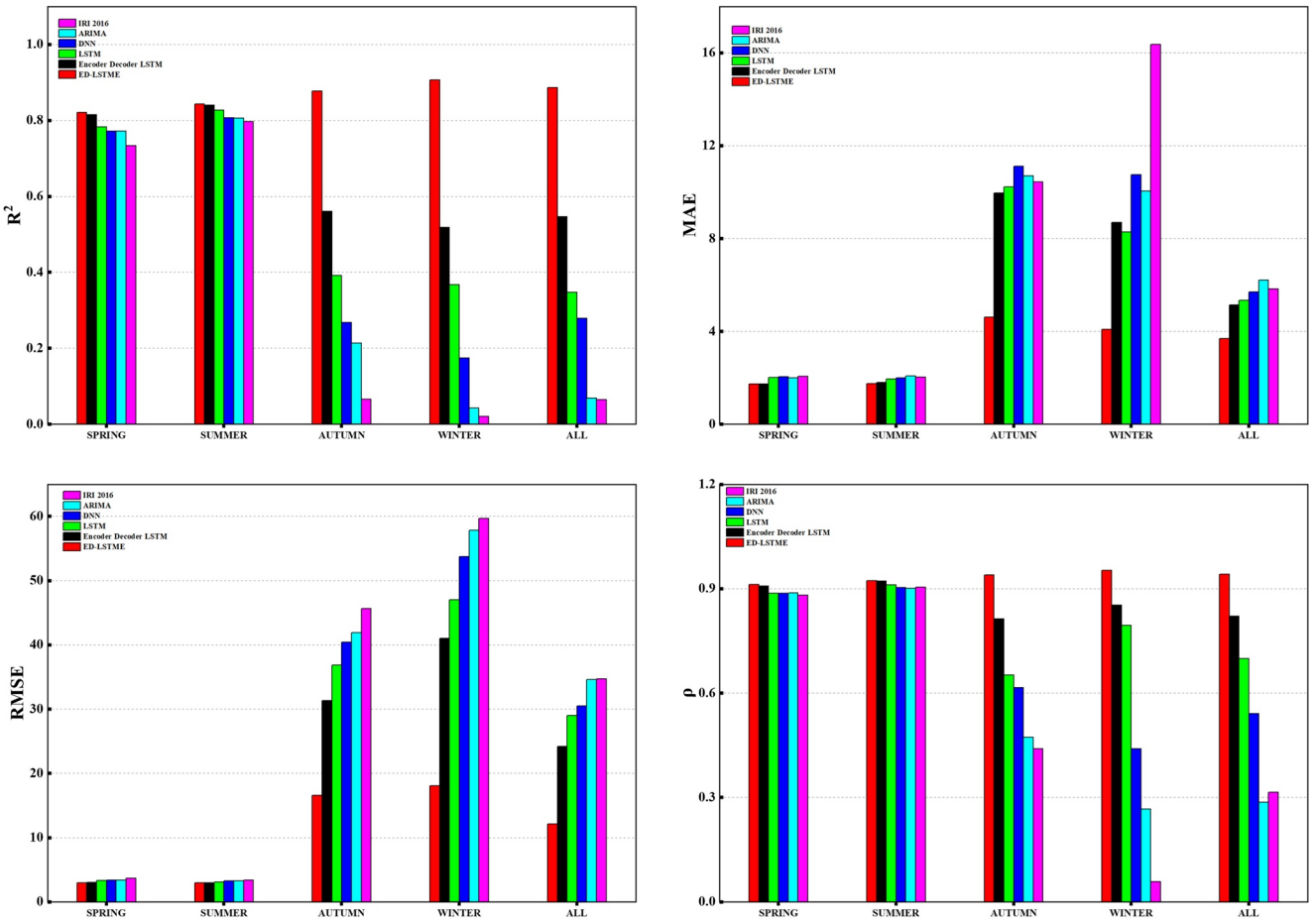

Figure 7. Seasonal variations in the R^2 (upper left), MAE (upper right), RMSE (lower left), and ρ (lower right) values between measured and predicted TEC values using the ED-LSTME, encoder–decoder LSTM, LSTM, DNN, ARIMA, and IRI 2016 models. ARIMA, autoregressive integrated moving average; DNN, deep neural network; ED-LSTME, encoder-decoder long short-term memory extended; IRI, International Reference Ionosphere; LSTM, long short-term memory; MAE, mean absolute error; RMSE, root mean square error; TEC, total electron content.

Tables S5 and S6 and Figure 8 present the specific errors of the models. The ED-LSTME model yielded the best prediction results based on the comparison of errors for quiet days and disturbed conditions. Under disturbed conditions, the RMSE increased by 5.04/1.89 TECU (K_p/a_p), and the R^2 value decreased by 0.11/0.08 TECU (K_p/a_p). The other five models exhibited diverse changes. Notably, only the ED-LSTME model could accurately capture complex trends during storms and other geomagnetic disturbances, likely because this model considered solar and geomagnetic activity values as input data. In order to further verify whether the performance can be improved by adding auxiliary input, extended LSTM (LSTME) and extended DNN (DNNE) models have been developed by adding solar and geomagnetic activity values as auxiliary inputs. Taylor diagrams in Figure S2 shows that both the error standard deviation and correlation of LSTME and DNNE performed better than that of LSTM and DNN, respectively. The biases are also less in the LSTME and DNNE models. Overall, the ED-LSTME is still the best performing model and shows a strong capability in TEC forecasting across the solar and geomagnetic activity.

Further, to better verify the effectiveness of the proposed ED-LSTME model, we selected four quiet days (days with a K_p index under 3.0) in spring (March 11, 2017), summer (August 16, 2017), autumn (September 10, 2017), and winter (December 10, 2017) as test cases. The TEC results obtained using the proposed ED-LSTME model, encoder-decoder LSTM, LSTM, ARIMA, and IRI 2016 models, NeQuick model (Nava et al., 2008), and GPS observations at 15 stations are compared in Figure 9. Twelve stations covering different geographical locations were selected, including WUSH, HRBN, TASH, and SUIY stations at high latitudes; YANC, LUZH, TAIN, and XNIN at midlatitudes; and KMIN, XIAM, QION, and XIAG at low latitudes.

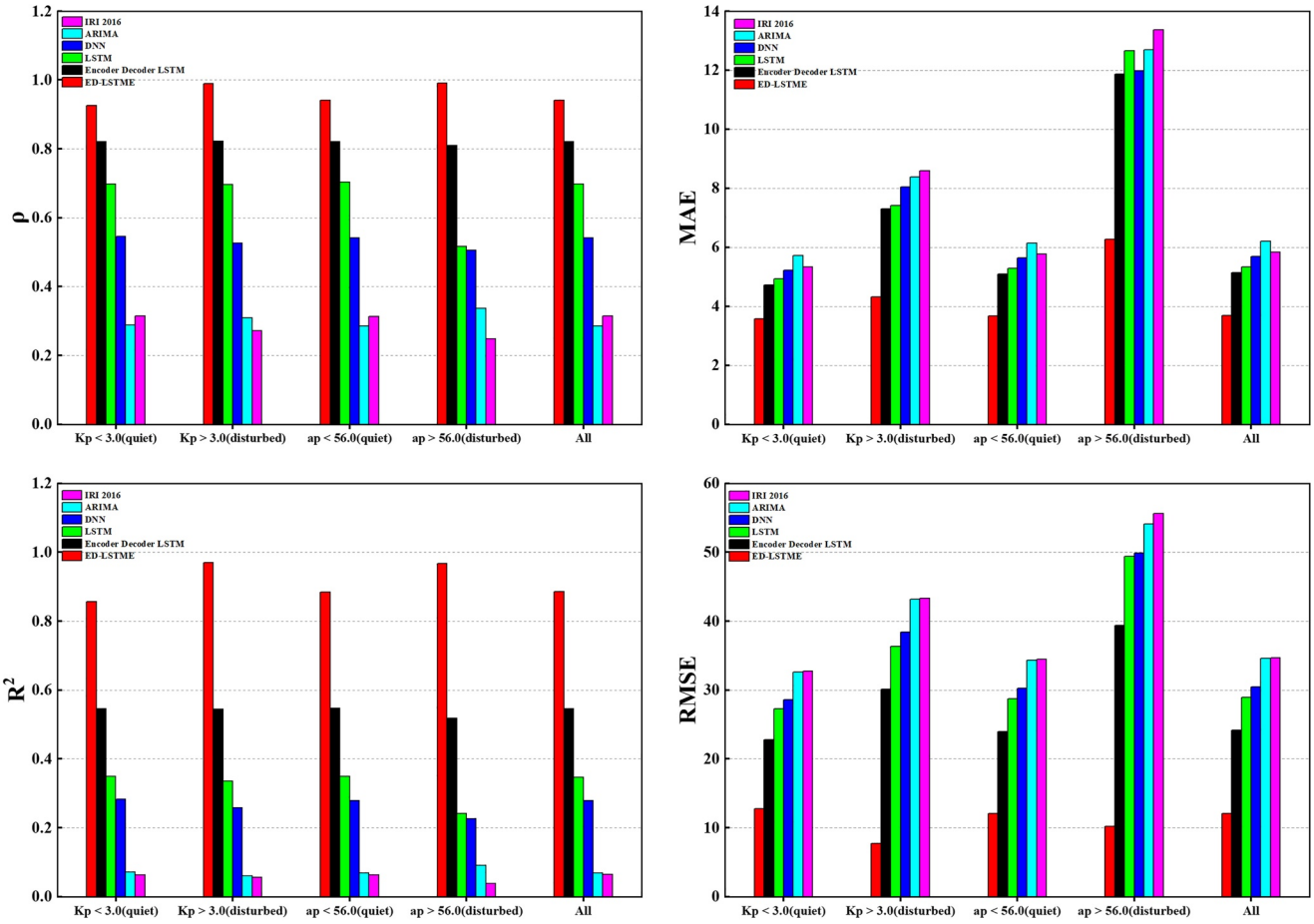

Figure 8. Bar graphs of the R^2 (upper left), MAE (upper right), RMSE (lower left), and ρ (lower right) between GPS-measured TEC values and the predicted values under varying solar and geomagnetic activity levels in 2017. MAE, mean absolute error; RMSE, root mean square error; TEC, total electron content.

Figure 9 demonstrates that the TEC estimated by the ED-LSTME model agrees with the observed TEC, implying that the model is notably superior to other methods with respect to capturing diurnal variations in TEC, while NeQuick and IRI 2016 models only captured the overall trends of the actual data. At low-latitude stations such as XIAM and XIAG, model performance was weaker due to the EIA.

To study the prediction performance of the models under conditions of geomagnetic disturbance, we selected four intense geomagnetic storms (with $K_p > 3.0$) in 2017 and analyzed their effects on the predicted TEC. These storm events (K_p index above 3.0) occurred on March 2 (spring), August 19 (summer), September 8 (autumn), and December 5 (winter). Figure S1 shows that the ED-LSTME model could predict the TEC disturbances associated with these geomagnetic storms for all stations. The ED-LSTME model's performance was particularly strong at WUSH, YANC, and KMIN stations and was typically better in spring than in winter.

The uncertainty of the proposed ED-LSTME model is shown in Figure 9 and Figure S1. We calculated the standard deviation between the results obtained using the proposed ED-LSTME model and GPS observations and considered the result to represent the uncertainty of the proposed ED-LSTME model. As parameter tuning of the proposed deep-learning model is time-consuming and challenging, we cannot guarantee that optimized parameters were obtained for the models trained at each GPS station; however, most cases were covered through the grid search method employed in our study. Still, this introduced additional uncertainty to the TEC forecasts of the proposed model.

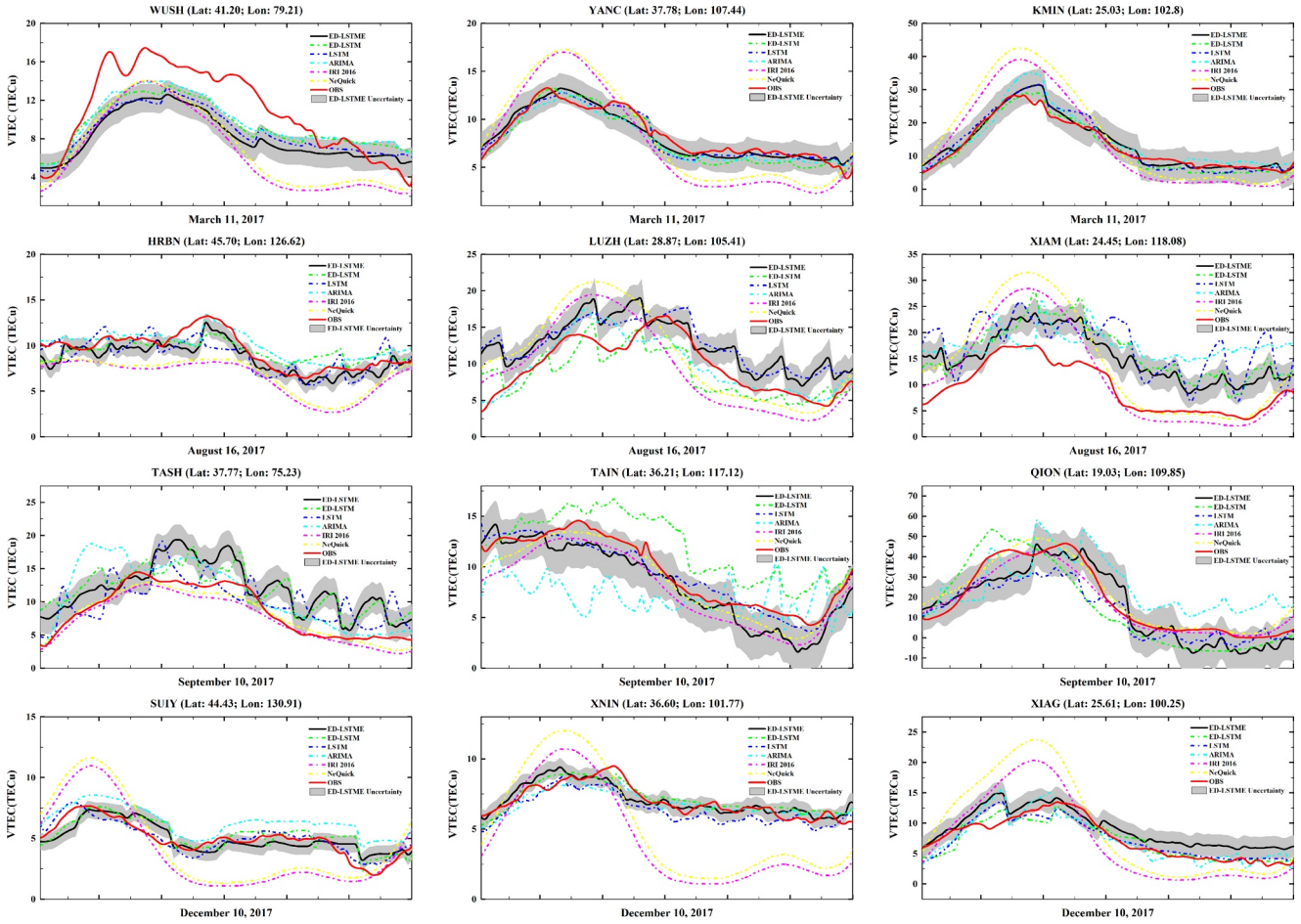

Figure 9. Comparison of the TECs predicted by the ED-LSTME (black solid line), ED-LSTM (green short dashed dot), LSTM (blue short dashed dot), ARIMA (cyan short dashed dot), IRI 2016 (magenta short dashed dot), and NeQuick (yellow short dashed dot) models and that recorded in GPS data (red solid line) from 15 different stations during quiet periods on March 11 (spring), August 16 (summer), September 10 (autumn), and December 10 (winter), 2017. ARIMA, autoregressive integrated moving average; ED-LSTME, encoder-decoder long short-term memory extended; IRI, International Reference Ionosphere; LSTM, long short-term memory; TEC, total electron content.

4.5. Discussion

The results imply that all the tested deep-learning models had high learning levels and prediction abilities, with potential variations owing to their diverse learning methods (Tien et al., 2020). The deep-learning models were more flexible than conventional models with respect to nonlinear learning, particularly of large datasets, although their implementation was more complex than that of traditional machine-learning models. In conventional machine-learning models, most input features require expert classification to reduce the complexity of the data and make the patterns more accessible to the learning algorithms. In contrast, the deep-learning models incrementally learned to extract high-level features from the data, negating the need for expert feature classification.

Although the results of this study confirmed that LSTM-based deep-learning models can be used for short-term predictions (e.g., using one-day historical input TEC data to forecast 3 h of TEC data), future studies should focus on the capability of deep-learning models to estimate TEC in the medium and long terms. Preprocessing methods, such as the combination of wavelet decomposition with deep-learning models, could also be explored for TEC forecasting. Decomposition methods can be utilized to remove noise from the data, improving the model accuracy. Furthermore, the hybrid CNN–LSTM model, deep reinforcement learning, generative adversarial network, and other deep-learning models should also be explored. Moreover, the storm-time ionospheric prediction is usually related to seasonal variation. Tang et al. (2020) found

that the LSTM-based ionospheric storm-time prediction model shows a significant dependence on seasonal variation, which provides a new dimension for our future research.

5. Conclusions

In this study, an ED-LSTME model was proposed to predict ionospheric TEC based on historical TEC, solar flux, and geomagnetic-activity data, and it demonstrated good performance in modeling time series with long time dependencies and in identifying optimum time lags and prediction horizons. To evaluate the performance of the proposed model, 15-min TECs from GPS measurements over one solar cycle were collected from 15 GPS stations in China. The same datasets were used to compare six different models: ED-LSTME, encoder-decoder LSTM, LSTM, DNN, ARIMA, and IRI 2016. The models were trained using optimal hyperparameters. Regarding R^2, RMSE, MAE, and correlation coefficient, the ED-LSTME outperforms the other algorithms, and compared with conventional models, such as ARIMA and IRI 2016, deep learning-based models delivered better prediction performance. In comparison with the DNN model, the proposed ED-LSTME, Encoder-Decoder LSTM, and conventional LSTM identify spatiotemporal correlations more effectively and deliver better prediction performances. The performances were significantly improved with the use of auxiliary data on solar flux and geomagnetic activity.

To more accurately assess the prediction performances of the models, geographical location, seasonal variation, and geomagnetic-activity variations were also considered as factors affecting TEC estimation. The RMSEs obtained for the six models were larger at low latitudes, which might have been due to the EIA. Data sets for each season were established to determine seasonal variations in model performances. The results revealed that the proposed model had good predictive power in each season and that seasonal observations were more suitable than annual observations. Under both quiet and disturbed conditions, the ED-LSTME model effectively predicted short-term changes in TEC during solar flux and geomagnetic events.

Long-term predictions are more difficult than short-term predictions, as they require more pertinent historical input data. Hence, the investigation of the performance of different deep-learning models to make medium- and long-term TEC predictions is recommended for future studies, as is the operational implementation of the proposed model.

Data Availability Statement

The GNSS data of CMONOC can be accessed from the platform of the GNSS data analysis center SHAO (SHA: http://www.shao.ac.cn/shao_gnss_ac). The geomagnetic activity index K_p was provided by the GFZ German Research Centre for Geosciences (https://www.gfz-potsdam.de/en/kp-index/). The solar activity index F10.7 was downloaded from SPDF OMNIWeb database (https://omniweb.gsfc.nasa.gov/form/dx1.html). The IRI-2016 and NeQuick-2 models are publicly available on http://irimodel.org and https://t-ict4d.ictp.it/nequick2/nequick-2-web-model, respectively.

Acknowledgments
This work was supported in part by the National Key R&D Program of China under Grant No. 2018YFC1503505 and in part by the Special Fund of the Institute of Earthquake Forecasting, China Earthquake Administration under Grant 2020IEF0510 and Grant 2020IEF0705.

References

Abadi, M., Barham, P., Chen, J., Chen, Z., Davis, A., Dean, J., et al. (2016). *Tensorflow: A system for large-scale machine learning*. Paper presented at the 12th USENIX Symposium on Operating Systems Design and Implementation.

Acharya, R., Roy, B., Sivaraman, M. R., & Dasgupta, A. (2011). Prediction of ionospheric total electron content using adaptive neural network with in-situ learning algorithm. *Advances in Space Research*, *47*(1), 115–123. https://doi.org/10.1016/j.asr.2010.08.016

Afraimovich, E. L., Altyntsev, A. T., Kosogorov, E. A., Larina, N. S., & Leonovich, L. A. (2001). Ionospheric effects of the solar flares of September 23, 1998 and July 29, 1999 as deduced from global GPS network data. *Journal of Atmospheric and Solar-Terrestrial Physics*, *63*(17), 1841–1849. https://doi.org/10.1016/s1364-6826(01)00060-8

Badeke, R., Borries, C., Hoque, M. M., & Minkwitz, D. (2018). Empirical forecast of quiet time ionospheric total electron content maps over Europe. *Advances in Space Research*, *61*(12), 2881–2890. https://doi.org/10.1016/j.asr.2018.04.010

Bartels, J., & Veldkamp, J. (1949). International data on magnetic disturbances, first quarter, 1949. *Journal of Geophysical Research*, *54*(3), 295–299. https://doi.org/10.1029/jz054i003p00295

Belehaki, A., Stanislawska, I., & Lilensten, J. (2009). An overview of ionosphere—Thermosphere models available for space weather purposes. *Space Science Reviews*, *147*(3–4), 271–313. https://doi.org/10.1007/s11214-009-9510-0

Bent, R. B., Llewellyn, S. K., Nesterczuk, G., & Schmid, P. (1975). The development of a highly-successful worldwide empirical ionospheric model and its use in certain aspects of space communications and worldwide total electron content investigations. In J. M. Goodman (Ed.), *Effect of the ionosphere on space systems and communications* (Vol. 1, pp. 13–28). Naval Research Laboratory.

Bilitza, D. (2001). International reference ionosphere 2000. *Radio Science*, *36*(2), 261–275. https://doi.org/10.1029/2000rs002432

Bilitza, D. (2018). IRI the international standard for the ionosphere. *Advances in Radio Science*, *16*, 1–11. https://doi.org/10.5194/ars-16-1-2018

Bilitza, D., Altadill, D., Truhlik, V., Shubin, V., Galkin, I., Reinisch, B., & Huang, X. (2017). International reference ionosphere 2016: From ionospheric climate to real-time weather predictions. *Space Weather*, *15*(2), 418–429. https://doi.org/10.1002/2016sw001593

Blagoveshchensky, D. V., Maltseva, O. A., & Sergeeva, M. A. (2018). Impact of magnetic storms on the global TEC distribution. *Annales Geophysicae*, 36(4), 1057–1071. https://doi.org/10.5194/angeo-36-1057-2018

Chen, Z., Jin, M., Deng, Y., Wang, J. S., Huang, H., Deng, X., & Huang, C. M. (2019). Improvement of a deep learning algorithm for total electron content maps: Image completion. *Journal of Geophysical Research: Space Physics*, *124*(1), 790–800. https://doi.org/10.1029/2018ja026167

Cherrier, N., Castaings, T., & Boulch, A. (2017). *Forecasting ionospheric total electron content maps with deep neural networks*. Paper presented at the Proc. Conf. Big Data Space (BIDS), ESA Workshop.

Cho, K., van Merriënboer, B., Gulcehre, C., Bahdanau, D., Bougares, F., Schwenk, H., & Bengio, Y. (2014). *Learning phrase representations using RNN encoder-decoder for statistical machine translation*. Paper presented at the Proceedings of the 2014 Conference on Empirical Methods in Natural Language Processing (EMNLP), Doha, Qatar.

Choi, B. K., Cho, J. H., & Lee, S. J. (2011). Estimation and analysis of GPS receiver differential code biases using KGN in Korean Peninsula. *Advances in Space Research*, *47*(9), 1590–1599. https://doi.org/10.1016/j.asr.2010.12.021

Chollet, F. (2015). *Keras*. Retrieved from https://github.com/fchollet/keras

Chollet, F. (2017). *Deep learning with python*. Manning Publications Co. Retrieved from https://www.manning.com/books/deep-learning-with-python

Elmunim, N. A., Abdullah, M., Hasbi, A. M., & Bahari, S. A. (2017). Comparison of GPS TEC variations with Holt-Winter method and IRI-2012 over Langkawi, Malaysia. *Advances in Space Research*, *60*(2), 276–285. https://doi.org/10.1016/j.asr.2016.07.025

Elvidge, S., Angling, M. J., & Nava, B. (2014). On the use of modified Taylor diagrams to compare ionospheric assimilation models. *Radio Science*, *49*(9), 737–745. https://doi.org/10.1002/2014rs005435

Feizi, R., Voosoghi, B., & Reza Ghaffari Razin, M. (2020). Regional modeling of the ionosphere using adaptive neuro-fuzzy inference system in Iran. *Advances in Space Research*.

Ghaffari Razin, M. R., & Voosoghi, B. (2016). Wavelet neural networks using particle swarm optimization training in modeling regional ionospheric total electron content. *Journal of Atmospheric and Solar-Terrestrial Physics*, *149*, 21–30. https://doi.org/10.1016/j.jastp.2016.09.005

Ghaffari Razin, M. R., & Voosoghi, B. (2020). Ionosphere time series modeling using adaptive neuro-fuzzy inference system and principal component analysis. *GPS Solutions*, *24*(2). https://doi.org/10.1007/s10291-020-0964-6

Goodfellow, I., Bengio, Y., & Courville, A. (2016). *Deep learning*. MIT press. Retrieved From http://www.deeplearningbook.org

Goodman, J. M. (1992). *HF communication: Science & technology*. Van Nostrand Reinhold Company.

Habarulema, J. B., McKinnell, L.-A., & Cilliers, P. J. (2007). Prediction of global positioning system total electron content using Neural Networks over South Africa. *Journal of Atmospheric and Solar-Terrestrial Physics*, *69*(15), 1842–1850. https://doi.org/10.1016/j.jastp.2007.09.002

Habarulema, J. B., McKinnell, L.-A., & Opperman, B. D. L. (2011). Regional GPS TEC modeling; Attempted spatial and temporal extrapolation of TEC using neural networks. *Journal of Geophysical Research*, *116*(A4). https://doi.org/10.1029/2010ja016269

Hernández-Pajares, M., García-Rigo, A., Juan, J. M., Sanz, J., Monte, E., & Aragón-Àngel, A. (2012). GNSS measurement of EUV photons flux rate during strong and mid solar flares. *Journal of Geophysical Research*, *10*(12). https://doi.org/10.1029/2012SW000826

Hernández-Pajares, M., Juan, J. M., Sanz, J., Aragón-Àngel, À., García-Rigo, A., Salazar, D., & Escudero, M. (2011). The ionosphere: effects, GPS modeling and the benefits for space geodetic techniques. *Journal of Geodesy*, *85*(12), 887–907. https://doi.org/10.1007/s00190-011-0508-5

Hinton, G. E., & Salakhutdinov, R. R. J. s. (2006). Reducing the dimensionality of data with neural networks. *Science*, *313*(5786), 504–507. https://doi.org/10.1126/science.1127647

Hochegger, G., Nava, B., Radicella, S., & Leitinger, R. (2000). A family of ionospheric models for different uses. *Physics and Chemistry of the Earth, Part C: Solar, Terrestrial & Planetary Science*, *25*(4), 307–310. https://doi.org/10.1016/s1464-1917(00)00022-2

Hochreiter, S., & Schmidhuber, J. (1997). Long short-term memory. *Neural Computation*, *9*(8), 1735–1780. https://doi.org/10.1162/neco.1997.9.8.1735

Hu, Y.-L., & Chen, L. (2018). A nonlinear hybrid wind speed forecasting model using LSTM network, hysteretic ELM and Differential Evolution algorithm. *Energy Conversion and Management*, *173*, 123–142. https://doi.org/10.1016/j.enconman.2018.07.070

Huang, Z., Li, Q. B., & Yuan, H. (2015). Forecasting of ionospheric vertical TEC 1-h ahead using a genetic algorithm and neural network. *Advances in Space Research*, *55*(7), 1775–1783. https://doi.org/10.1016/j.asr.2015.01.026

Huang, Z., & Yuan, H. (2014). Ionospheric single-station TEC short-term forecast using RBF neural network. *Radio Science*, *49*(4), 283–292. https://doi.org/10.1002/2013rs005247

Hyndman, R. J., & Athanasopoulos, G. (2018). *Forecasting: Principles and practice*. Melbourne, Australia: OTexts. Retrieved from OTexts.com/fpp2

Hyndman, R. J., & Khandakar, Y. (2008). Automatic time series forecasting: The forecast Package for R. *Journal of Statistical Software*, *27*(3), 22. https://doi.org/10.18637/jss.v027.i03

Kaselimi, M., Voulodimos, A., Doulamis, N., Doulamis, A., & Delikaraoglou, D. (2020). A causal long short-term memory sequence to sequence model for TEC prediction using GNSS observations. *Remote Sensing*, *12*(9). https://doi.org/10.3390/rs12091354

Kersley, L., Malan, D., Pryse, S. E., Cander, L. R., Bamford, R. A., Belehaki, A., et al. (2004). Total electron content-A key parameter in propagation: Measurement and usein ionospheric imaging. *Annals of Geophysics*, *47*(2–3 Sup.).

Krankowski, A., Kosek, W., Baran, L. W., & Popinski, W. (2005). Wavelet analysis and forecasting of VTEC obtained with GPS observations over European latitudes. *Journal of Atmospheric and Solar-Terrestrial Physics*, *67*(12), 1147–1156. https://doi.org/10.1016/j.jastp.2005.03.004

Kumar, S., & Singh, A. (2010). *The effect of geomagnetic storm on GPS derived total electron content (TEC) at Varanasi, India*. Paper presented at the Journal of Physics: Conference Series.

LeCun, Y., Bengio, Y., & Hinton, G. (2015). Deep learning. *Nature*, *521*(7553), 436–444. https://doi.org/10.1038/nature14539. Retrieved from https://www.ncbi.nlm.nih.gov/pubmed/26017442

Li, J., Huang, D., Wang, Y., Zhao, Y., & Hassan, A. (2020). A new model for total electron content based on ionospheric continuity equation. *Advances in Space Research*.

Li, Z., Yuan, Y., Li, H., Ou, J., & Huo, X. (2012). Two-step method for the determination of the differential code biases of COMPASS satellites. *Journal of Geodesy*, *86*(11), 1059–1076. https://doi.org/10.1007/s00190-012-0565-4

Ma, G., & Maruyama, T. (2003). Derivation of TEC and estimation of instrumental biases from GEONET in Japan. *Annales Geophysicae*, *21*(10), 2083–2093. https://doi.org/10.5194/angeo-21-2083-2003

Makridakis, S., & Hibon, M. (1997). ARMA models and the Box-Jenkins methodology. *Journal of Forecasting*, *16*(3), 147–163. https://doi.org/10.1002/(sici)1099-131x(199705)16:3<147::aid-for652>3.0.co;2-x

Mannucci, A. J., Wilson, B. D., Yuan, D. N., Ho, C. H., Lindqwister, U. J., & Runge, T. F. (1998). A global mapping technique for GPS-derived ionospheric total electron content measurements. *Radio Science*, *33*(3), 565–582. https://doi.org/10.1029/97rs02707

Moreno, E., Rigo, A., Hernández-Pajares, M., & Yang, H. (2018). TEC forecasting based on manifold trajectories. *Remote Sensing*, *10*(7), 988. https://doi.org/10.3390/rs10070988

Moritz, S. (2016). *imputeTS: Time series missing value imputation*. R package version 1.7. Retrieved from http://CRAN.R-project.org/package=imputeTS

Mukesh, R., Karthikeyan, V., Soma, P., & Sindhu, P. (2020). Forecasting of ionospheric TEC for different latitudes, seasons and solar activity conditions based on OKSM. *Astrophysics and Space Science*, *365*(1). https://doi.org/10.1007/s10509-020-3730-x

Mukhtarov, P., Pancheva, D., & Andonov, B. (2014). Hybrid model for long-term prediction of the ionospheric global TEC. *Journal of Atmospheric and Solar-Terrestrial Physics*, *119*, 1–10. https://doi.org/10.1016/j.jastp.2014.05.009

Nava, B., Coïsson, P., & Radicella, S. M. (2008). A new version of the NeQuick ionosphere electron density model. *Journal of Atmospheric and Solar-Terrestrial Physics*, *70*(15), 1856–1862. https://doi.org/10.1016/j.jastp.2008.01.015

Nava, B., Radicella, S. M., & Azpilicueta, F. (2011). Data ingestion into NeQuick 2. *Radio Science*, *46*(6). https://doi.org/10.1029/2010rs004635

Okoh, D., Owolabi, O., Ekechukwu, C., Folarin, O., Arhiwo, G., Agbo, J., et al. (2016). A regional GNSS-VTEC model over Nigeria using neural networks: A novel approach. *Geodesy and Geodynamics*, *7*(1), 19–31. https://doi.org/10.1016/j.geog.2016.03.003

Orus Perez, R. (2019). Using TensorFlow-based Neural Network to estimate GNSS single frequency ionospheric delay (IONONet). *Advances in Space Research*, *63*(5), 1607–1618. https://doi.org/10.1016/j.asr.2018.11.011

Pei, S., Niu, F., Ben-Zion, Y., Sun, Q., Liu, Y., Xue, X., et al. (2019). Seismic velocity reduction and accelerated recovery due to earthquakes on the Longmenshan fault. *Nature Geoscience*, *12*(5), 387–392. https://doi.org/10.1038/s41561-019-0347-1

Purohit, P., Mansoori, A. A., Khan, P. A., Atulkar, R., Bhawre, P., Tripathi, S. C., et al. (2015). *Evaluation of geomagnetic storm effects on the GPS derived total electron content (TEC)*. Paper presented at the Journal of Physics: Conference Series.

Qing, X., & Niu, Y. (2018). Hourly day-ahead solar irradiance prediction using weather forecasts by LSTM. *Energy*, *148*, 461–468. https://doi.org/10.1016/j.energy.2018.01.177

Rawer, K., Bilitza, D., & Ramakrishnan, S. (1978). Goals and status of the International Reference Ionosphere. *Reviews of Geophysics*, *16*(2), 177–181. https://doi.org/10.1029/rg016i002p00177

Razin, M. R. G., Voosoghi, B., & Mohammadzadeh, A. (2015). Efficiency of artificial neural networks in map of total electron content over Iran. *Acta Geodaetica et Geophysica*, *51*(3), 541–555. https://doi.org/10.1007/s40328-015-0143-3

Ruwali, A., Kumar, A. J. S., Prakash, K. B., Sivavaraprasad, G., & Ratnam, D. V. (2020). Implementation of hybrid deep learning model (LSTM-CNN) for ionospheric TEC forecasting using GPS data. *IEEE Geoscience and Remote Sensing Letters*, 1–5. https://doi.org/10.1109/lgrs.2020.2992633

Samardjiev, T., Bradley, P. A., Cander, L. R., & Dick, M. I. (1993). Ionospheric mapping by computer contouring techniques. *Electronics Letters*, *29*(20), 1794–1795. https://doi.org/10.1049/el:19931194

Song, R., Zhang, X., Zhou, C., Liu, J., & He, J. (2018). Predicting TEC in China based on the neural networks optimized by genetic algorithm. *Advances in Space Research*, *62*(4), 745–759. https://doi.org/10.1016/j.asr.2018.03.043

Srivani, I., Siva Vara Prasad, G., & Venkata Ratnam, D. (2019). A deep learning-based approach to forecast ionospheric delays for GPS signals. *IEEE Geoscience and Remote Sensing Letters*, *16*(8), 1180–1184. https://doi.org/10.1109/lgrs.2019.2895112

Sutskever, I., Vinyals, O., & Le, Q. V. (2014). Sequence to sequence learning with neural networks (2). Paper presented at the Proceedings of the 27th International Conference on Neural Information Processing Systems, Montreal, Canada.

Tang, R., Zeng, F., Chen, Z., Wang, J.-S., Huang, C.-M., & Wu, Z. (2020). The comparison of predicting storm-time ionospheric TEC by three methods: ARIMA, LSTM, and Seq2Seq. *Atmosphere*, *11*(4), 316. https://doi.org/10.3390/atmos11040316

Taylor, K. E. (2001). Summarizing multiple aspects of model performance in a single diagram. *Journal of Geophysical Research*, *106*(D7), 7183–7192. https://doi.org/10.1029/2000jd900719

Tebabal, A., Radicella, S. M., Damtie, B., Migoya-Orue', Y., Nigussie, M., & Nava, B. (2019). Feed forward neural network based ionospheric model for the East African region. *Journal of Atmospheric and Solar-Terrestrial Physics*, *191*, 105052. https://doi.org/10.1016/j.jastp.2019.05.016

Tebabal, A., Radicella, S. M., Nigussie, M., Damtie, B., Nava, B., & Yizengaw, E. (2018). Local TEC modeling and forecasting using neural networks. *Journal of Atmospheric and Solar-Terrestrial Physics*, *172*, 143–151. https://doi.org/10.1016/j.jastp.2018.03.004

Tien Bui, D., Hoang, N. D., Martinez-Alvarez, F., Ngo, P. T., Hoa, P. V., Pham, T. D., et al. (2020). A novel deep learning neural network approach for predicting flash flood susceptibility: A case study at a high frequency tropical storm area. *The Science of the Total Environment*, *701*, 134413. https://doi.org/10.1016/j.scitotenv.2019.134413. Retrieved from https://www.ncbi.nlm.nih.gov/pubmed/31706212

Uwamahoro, J. C., & Habarulema, J. B. (2015). Modeling total electron content during geomagnetic storm conditions using empirical orthogonal functions and neural networks. *Journal of Geophysical Research: Space Physics*, *120*(12), 11000–11012. https://doi.org/10.1002/2015ja021961

Verkhoglyadova, O. P., Tsurutani, B. T., Mannucci, A. J., Mlynczak, M. G., Hunt, L. A., & Runge, T. (2013). Variability of ionospheric TEC during solar and geomagnetic minima (2008 and 2009): external high speed stream drivers. *Annales Geophysicae*, 31(2), 263–276. https://doi.org/10.5194/angeo-31-263-2013

Watthanasangmechai, K., Supnithi, P., Lerkvaranyu, S., Tsugawa, T., Nagatsuma, T., & Maruyama, T. (2012). TEC prediction with neural network for equatorial latitude station in Thailand. *Earth, Planets and Space*, *64*(6), 473–483. https://doi.org/10.5047/eps.2011.05.025

Xiaohong, Z., Xiaodong, R., Fengbo, W., & Qi, L. (2014). Short-term TEC Prediction of Ionosphere Based on ARIMA Model. *Acta Geodaetica et Cartographica Sinica*, *43*(2), 118–124.

Xiong, B., Wan, W., Ning, B., Ding, F., Hu, L., & Yu, Y. (2014). A statistic study of ionospheric solar flare activity indicator. *Space Weather*, *12*(1), 29–40. https://doi.org/10.1002/2013sw001000

Xiong, B., Wan, W., Yu, Y., & Hu, L. (2016). Investigation of ionospheric TEC over China based on GNSS data. *Advances in Space Research*, *58*(6), 867–877. https://doi.org/10.1016/j.asr.2016.05.033

Yang, G., Lee, H., & Lee, G. (2020). A hybrid deep learning model to forecast particulate matter concentration levels in Seoul, South Korea. *Atmosphere*, *11*(4), 348. https://doi.org/10.3390/atmos11040348

Yuan, Y., Li, Z., Wang, N., Zhang, B., Li, H., Li, M., et al. (2015). Monitoring the ionosphere based on the Crustal Movement Observation Network of China. *Geodesy and Geodynamics*, *6*(2), 73–80. https://doi.org/10.1016/j.geog.2015.01.004

Zhai, D.-l., Zhang, X.-m., Xiong, P., & Rui, S. (2019). Detection of ionospheric TEC anomalies based on prophet time-series forecasting model. *Earthquake*, *39*(2), 46–62.Retrieved from http://dizhen.ief.ac.cn/CN/abstract/article_58.shtml

Zhang, X.-H., Ren, X.-D., Feng-Bo, W. U., & Chen, Y.-Y. (2013). A new method for detection of pre-earthquake ionospheric anomalies. *Chinese Journal of Geophysics*, *56*(2), 441–449. https://doi.org/10.1002/cjg2.20021. Retrieved from http://www.geophy.cn//CN/abstract/article_9290.shtml

Zhao, Z., Chen, W., Wu, X., Chen, P. C. Y., & Liu, J. (2017). LSTM network: A deep learning approach for short-term traffic forecast. *IET Intelligent Transport Systems*, *11*(2), 68–75. https://doi.org/10.1049/iet-its.2016.0208

Zhukov, A. V., Yasyukevich, Y. V., & Bykov, A. E. (2020). GIMLi: Global ionospheric total electron content model based on machine learning. *GPS Solutions*, *25*(1). https://doi.org/10.1007/s10291-020-01055-1

Zivot, E., & Wang, J. (2003). Rolling analysis of time series. In *Modeling financial time series with S-Plus®* (pp. 299–346). New York, NY: Springer.